
Proceedings Paper:
Christofidou, K.A. orcid.org/0000-0002-8064-5874, Pang, H.T., Li, W. et al. (4 more authors) (2020) Microstructural control and optimization of Haynes 282 manufactured through laser powder bed fusion. In: Superalloys 2020 : Proceedings of the 14th International Symposium on Superalloys. 14th International Symposium on Superalloys 2020 Minerals, Metals & Materials Series . Springer International Publishing , pp. 1014-1023. ISBN 9783030518332

https://doi.org/10.1007/978-3-030-51834-9_99

Microstructural control and optimisation of Haynes 282 manufactured through laser powder bed fusion

K.A. Christofidou[1&2], H. T. Pang[1], W. Li[3], Y. Pardhi[3&4], C.N. Jones[3], N.G. Jones[1] and H. J. Stone[1*]

[1]Dept. of Materials Science and Metallurgy, University of Cambridge, 27 Charles Babbage Road, CB3 0FS, UK

[2] Now at: Department of Materials Science and Engineering, The University of Sheffield,
Sir Robert Hadfield Building, Mappin Street, Sheffield S1 3JD, UK

[3]Rolls-Royce plc, PO Box 31, Derby, DE24 8BJ, UK

[4]Now at: Sulzer Ltd., Manor Mill Lane, Leeds, UK, LS11 8BR, UK
*Corresponding author: Dr Howard J. Stone, hjs1002@cam.ac.uk

Abstract
The microstructure and properties of alloy Haynes 282 produced through laser powder bed fusion were investigated as a function of the post-deposition heat-treatment. Scanning electron microscopy and X-ray diffraction were utilised to characterize the microstructure, whilst electro-thermal mechanical testing was used to evaluate the tensile and creep properties at 900˚C. In the as-deposited state, the initial microstructure consisted of the γ and γ′ phases along with M_6C and $M_{23}C_6$ carbides. These carbides were observed to govern the recrystallization behavior of the material and resulted in a minimum recrystallization temperature of 1240˚C. Following post-deposition heat-treatments the microstructures consisted of a monomodal distribution of γ′ with M_6C and $M_{23}C_6$ carbides along the grain boundaries. Tertiary γ′ particles were found to form in the vicinity of carbides in samples that employed a γ′ super-solvus step prior to ageing at 788˚C. The tensile properties were found to be similar in all heat-treated states, consistent with the minimal differences observed in the microstructures. In contrast, significant differences in the creep behavior of the alloy was observed following the different heat-treatments, although no correlation with the microstructures was observed.

Keywords: Haynes 282, laser powder bed fusion, mechanical properties, heat-treatments, recrystallization

Introduction
The ability to produce parts with complex geometries, inaccessible through traditional fabrication methods, has made additive manufacturing (AM) an enabling process for many industries [1]. This is of particular significance for gas turbine components, where the fine control of complex cooling channels and intricate part geometries can provide marked improvements to engine efficiency [2]. The extreme conditions encountered within gas turbines necessitate the use of Ni-based superalloys. However, superalloys with high γ′ volume fractions often suffer from cracking during AM and, as such, alloys with lower γ′ fractions are favored [3, 4]. In addition, industrial uptake of AM Ni-based superalloys is further limited by the difficulties encountered in controlling the resulting microstructures, and hence properties, following deposition [5]. Specifically, the thermal profiles that the materials encounter during manufacturing lead to non-equilibrium structures that require modification through post-processing heat-treatments in order to tailor the resulting mechanical properties and allow reliable lifing operations to take place.

In this work, the microstructural optimization of the Ni-based superalloy Haynes 282 (H282) manufactured through laser powder bed fusion (LPBF) is reported. H282 was developed to offer a good combination of creep resistance, thermal stability and weldability, for applications in the temperature range ~650-930˚C [6, 7]. In order to achieve these properties, high concentrations of solid solution strengthening elements, in particular Mo, were utilized, whilst also limiting the concentrations of γ′ forming elements such that the fraction of γ′ was ~20-30% for improved weldability [6, 7]. The optimal microstructure is produced through a three-step heat-treatment. First, a γ′ and $M_{23}C_6$ super solvus solution step is used to homogenize the material followed by rapid cooling. Second, an initial aging step at 1010˚C, which is above the γ′ solvus temperature, is used to aid the formation of the $M_{23}C_6$ carbides at the grain boundaries. Third, a final ageing step is performed at 788˚C to precipitate the γ′ phase with an appropriate particle size distribution [7, 8]. On completion of this multi-step heat-treatment, the microstructure comprises large MC/MN, Ti-rich carbides/nitrides as well as $M_{23}C_6$ and M_6C carbides and a monomodal γ′ distribution with a mean size of ~20 nm [7, 9, 10]. This microstructure has been reported to remain stable following prolonged exposures at 870˚C [10].

Unocic *et al.* [11], investigated the alloy following fabrication using electron beam melting (EBM). Unlike conventionally cast material, grain boundary carbides were observed in the as-deposited state. However, these carbides were found to be Ti-Mo-rich MC-type carbides rather than $M_{23}C_6$. Furthermore, the mean γ′ size obtained in the as-deposited EBM material was ~120 nm, compared to 20 nm obtained in the cast material. Heat-treatment of the material for 4 hours at 800˚C or following the conventional Haynes heat-treatment restored the γ′ distribution to 20-30 nm [11].

Whilst the alloy and its microstructures have been studied in the cast and EBM state and following long duration exposures at high temperatures, little is known about the microstructures and properties of the material following LPBF or about the effect of post-

deposition heat-treatments. Therefore, this study aims to understand the alloy in greater detail and explore the sensitivity of the mechanical properties to such post-deposition heat-treatments.

Experimental Methods

Defect free coupons of H282 were manufactured by LPBF on an EOS M280 instrument using virgin powder with particle sizes up to 45 μm and composition shown in Table 1. Two coupon geometries were used, and the build parameters were kept constant for all samples to allow meaningful comparisons of the effect of post-processing operations. Coupons 30 mm by 30 mm and 1 mm thick were used in the analyses of the microstructural evolution, whilst bespoke miniature bowtie specimens were built for mechanical testing. In order to avoid any interactions with the stainless-steel baseplate samples were built on a supporting plinth 3.5 mm high.

Table 1: Composition of Haynes 282® powder investigated in this study

Element	**Ni**	**Co**	**Cr**	**Mo**	**Al**	**Ti**	**C**	**B**
wt%	Bal.	10.8	19.3	8.0	1.5	2.1	0.06	0.004
at.%	Bal.	10.6	21.4	4.8	3.2	2.6	0.29	0.021

Differential scanning calorimetry (DSC) was performed on as-deposited coupons in order to identify the key transition temperatures. A 5 mm diameter disc was extracted from 1 mm thick coupons using electron discharge machining (EDM) and tested on a Netzsch 404 DSC operated at 10˚C/min heating/cooling rates under flowing argon. The resulting data were analysed using the first deviation from baseline approach [12] and a liquidus temperature of ~1390˚C, a solidus temperature of ~ 270˚C and a γ′ solvus temperature of ~1000˚C were identified.

A series of heat-treatments were performed on the material in order to identify a set of post-processing parameters that resulted in optimum mechanical performance. Table 2 summarizes the heat-treatments considered. Heat-treatments A and B were performed industrially by Rolls-Royce plc. and are modelled after the heat-treatments suggested by Haynes for wrought material [6]. Sand blasting was only utilised in the industrial heat-treatments as this is a standard post-processing step used to reduce the surface roughness on as-build components and does not alter the bulk sample microstructures. The remaining heat-treatments detailed in Table 2 were performed in laboratory equipment, with samples inserted into a hot furnace. In order to minimise environmental interactions during the heat-treatments, these samples were encapsulated in argon backfilled quartz ampoules.

Table 2: Heat-treatment recipes performed on as-deposited Haynes 282® samples. Gas fan quenching (GFQ) cooling rates equivalent to 0.5-0.9 ˚C/s and furnace cooling (FC) refers equivalent to cooling 4 ˚C per minute. AC refers to Air Cooling and RT to Room Temperature.

Heat-treatment	**Details**
A	Sand blasted + 1150 ˚C/1 hour (a ramp up rate of ~ 3-4 ˚C per minute was used)
B	Sand blasted + 1150 ˚C/1 hour + 1010 ˚C/4 hours + 788 ˚C/8 hours (a ramp up rate of ~ 3-4 ˚C per minute was used)
C	1250 ˚C/1 hour + 1010 ˚C/2 hours + 788 ˚C/8 hours, GFQ to RT between each step
D	1250 ˚C/1 hour, FC to 788 ˚C, 788 ˚C/8 hours, GFQ to RT
E	1240˚ C/1 hour, FC to 788 ˚C, 788 ˚C/8 hours, AC to RT
F	1260 ˚C/1 hour, FC to 788 ˚C, 788 ˚C/8 hours, AC to RT
G	1250 ˚C/1 hour, FC to 990 ˚C, 990 ˚C/2 hours, FC to 788 ˚C, 788 ˚C/8 hours, AC to RT
H	1250 ˚C/1 hour, FC to 900 ˚C, 900 ˚C/2 hours, FC to 788 ˚C, 788 ˚C/8 hours, AC to RT
I	1250 ˚C/1 hour, FC to 1010 ˚C, 1010 ˚C/2 hours, FC to 788 ˚C, 788 ˚C/8 hours, AC to RT

Samples for microstructural analysis were prepared using standard metallographic techniques culminating in a final polishing stage with 0.06 μm colloidal silica solution. Where required, samples were immersion etched using Kalling's solution [13] or

electrolytically etched in a 10% phosphoric acid solution at ~5 V. An FEI Nova NanoSEM 450 scanning electron microscope (SEM), housing a Bruker xFlash 100 energy dispersive X-ray spectroscopy (EDX) detector and an e-Flash^{1000} electron backscattered diffraction (EBSD) detector, was used to characterize the alloy microstructures. Complementary X-ray diffraction was performed using a Bruker D8 diffractometer with a Ni filtered Cu source, to enable the crystallographic identification of the phases present. Diffraction data were collected between 20 and 120° 2θ, whilst phase identification and lattice parameters were obtained using the Pawley method [14] in the TOPAS-Academic software.

An Electro-Thermal Mechanical Testing (ETMT) machine with ± 3.5 kN load capacity [15] was used to conduct tensile and creep testing at ~900˚C on the heat-treated samples. Tensile testing was performed with a 1 µm/s grip displacement rate to achieve an ~1 x 10^{-5} s^{-1} strain rate within the specimen gauge length. Creep testing was performed at 900˚C under 120MPa, to match published data on the properties to wrought H282, where the nominal creep life is ~ 100 hours.

Prisms of a bowtie geometry were built with the gauge of the bowtie specimens measuring 12 mm in length by 1.5 mm in width. Prior to testing, the prisms were encapsulated in Ar-backfilled quartz tubes and subjected to heat-treatments C-H quoted in Table 2. Following heat-treatment, the prisms were sliced into ~1 mm thick specimens using EDM. The flat surfaces as well as the gauge length of the specimens were subsequently ground using progressive grades of SiC paper down to a final finish of ~5 µm. Due to limited sample availability and the requirement for calibration samples, only a single test per condition could be performed, unless otherwise stated. An R-type thermocouple was spot-welded onto the centre for each sample to control the temperature/current during testing. Heating within an ETMT machine is achieved by passing direct current (DC) through the gauge length of the specimen, with feedback control from the thermocouple welded onto the centre of the gauge. The DC profile used to heat the samples to an equivalent temperature of 900˚C was calibrated prior to testing using dummy samples of H282 under zero-load.

Results

Initial Microstructures

SEM images of the LPBF microstructures, taken perpendicular to the build direction, of the material in the as deposited condition and following heat-treatments A and B (Table 2) are shown in Figure 1. As expected, the material was found to solidify with cellular grains forming epitaxially along the build direction, Figure 1a. Following exposure at 1150˚C for 1 hour, small, spherical dark-contrast particles were observed along cellular and high angle grain boundaries, Figure 1b. The additional two-step heat-treatment (B) of 1010˚C for 4 hours followed by 788˚C for 8 hours resulted in the formation of a bright-contrast phase along the high angle grain boundaries, Figure 1c. The dark contrast phase along the high-angle grain boundaries was also found to coarsen, whereas the same phase decorating the cellular boundaries did not exhibit further growth. EDX analysis of the grain boundary phases in condition B revealed the carbides to be Mo-rich (bright) and Cr-rich (dull grey), which corresponded to the M_6C and $M_{23}C_6$ carbides. By means of comparison, Pike [7] and Unocic *et* al. [9] reported on the baseline microstructure of conventionally cast and wrought H282 following the standard heat treatment of 1010˚C for 2 hours followed by 788˚C for 8 hours. It was found that the baseline microstructure comprises large MC/MN, Ti-rich carbides/nitrides as well as $M_{23}C_6$ and M_6C carbides forming along the grain boundaries and a monomodal γ′ distribution. Whilst the presence of a Ti-rich MC/MN type compound is routinely identified in cast and EBM H282 [7, 11, 16], this phase was not identified in any of the LPBF microstructures reported in this study. Importantly, the cellular grain structure was evident in all sub-images in Figure 1, indicating that the material had not undergone recrystallisation.

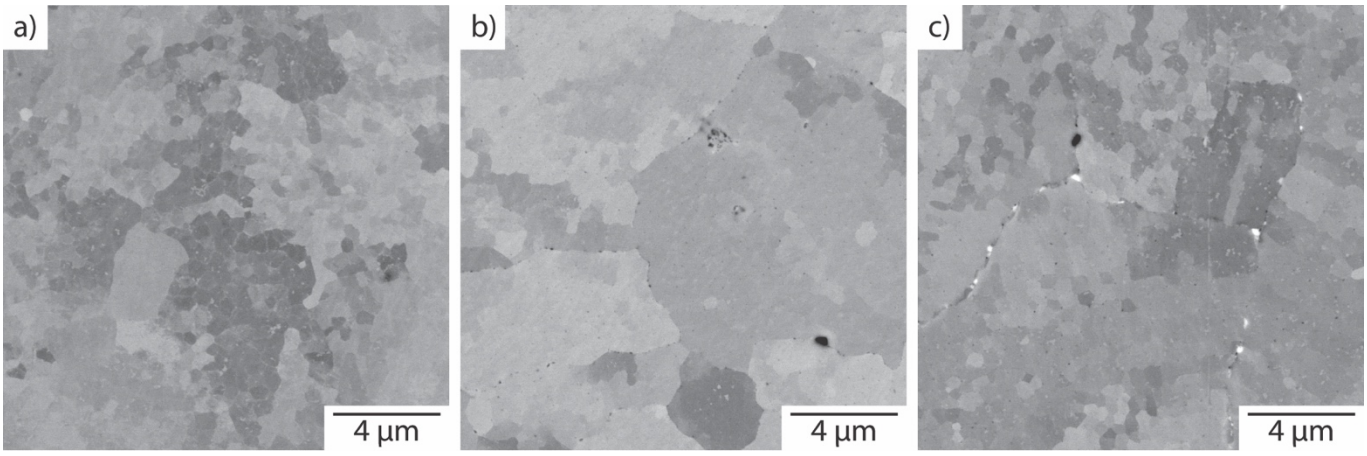

Figure 1: Back-scattered ***electron micrographs of alloy LPBF Haynes*** *282® in the transverse direction; a) As deposited condition, b) Sand blasted + 1150˚C/1 hour and c) Sand blasted + 1150˚C/1 hour + 1010˚C/4 hours + 788˚C/8 hours.*

Recrystallisation

Prior to the γ′ optimization heat-treatments outlined in Table 2, a series of exposures between 1150-1280°C and exposure times of up to 4 hours were carried out in order to identify a temperature at which full recrystallisation of the grain structure occurred. Backscattered imaging was used to evaluate the success of the different exposures in recrystallizing the grain structure. Once a successful set of conditions was identified, EBSD was performed to confirm and characterize the bulk grain structure. Partial recrystallisation was observed in samples exposed to 1190˚C for 1 hour, with a progressively higher fraction of recrystallized grains found with increasing temperature and exposure time until full recrystallisation was observed for samples exposed to 1250˚C for 1

hour, or 1240˚C for 2 hours. Figure 2 shows a comparison of the EBSD results collected in the form of an inverse pole figure colored map along the build direction. Figure 2a & b shows the strong texture present in the build direction in samples in the as-deposited condition (a) and following sand blasting and homogenization at 1150˚C/1 hour (b). In contrast, Figure 2c shows the recrystallized microstructure of the sample exposed to 1250˚C for 1 hour. The recrystallized microstructure also contained a large fraction of recrystallisation twins (~5 % by area). The average grain size obtained was ~75 µm, with an aspect ratio of ~2 biased towards the build direction.

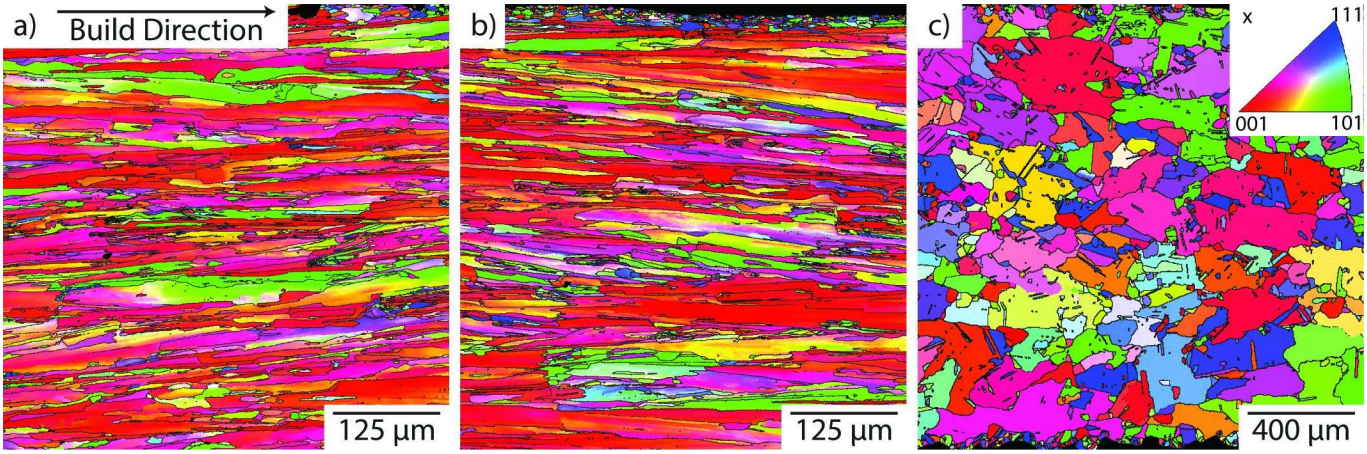

Figure 2: Inverse pole figure colored maps along the build direction (common for all samples) in the a) as-deposited condition, b) following sand blasting and heat-treatment at 1150˚C/1 hour and c) following a 1-hour exposure at 1250˚C. Note that for a full interpretation of the image the reader is referred to the colored digital version of the manuscript.

Heat-treated microstructures

The effect of heat-treatments C-I, Table 2, on the resulting microstructures of the alloy were also evaluated. A recrystallised microstructure was obtained in all of these samples that was consistent with the results presented in Figure 2c, although the exact grain size, aspect ratio and twin fraction was not evaluated for each condition. The characterisation studies performed focused instead on understanding the γ′ precipitate distributions as well as the grain boundary phases.

The γ′ distributions were characterised using SEM and image analysis, performed using data from several micrographs acquired in different grains, with a minimum of 1500 γ′ particles to allow for a statistically relevant sampling. These data was then described using a log-normal distribution as outlined by Goodfellow *et al.* [17]. It was found that heat-treatments D-I resulted in very similar γ′ distributions consisting of a uniform, monomodal dispersion of secondary precipitates. The mean particle sizes and standard deviations are shown in Table 3. Due to the faster cooling rates in heat-treatment C, the γ′ distribution could not be reliably quantified in this condition.

Table 3: Summary of the γ′ distributions obtained for heat-treatments D-I.

Heat-treatment	**D**	**E**	**F**	**G**	**H**	**I**
Mean size (nm)	97	104	83	105	93	102
Standard Deviation (nm)	36	43	31	43	34	43

SEM images of the extensive grain boundary precipitation that occurred during heat-treatments C-I are shown in Figure 3. Figure 3a presents the microstructure obtained from heat-treatment C. The faster cooling rates utilized resulted in a much finer distribution of γ′. The grain boundary precipitates were identified using XRD and were found to consist primarily of M_6C carbides with a small fraction of M_3B_2 borides. The grain boundary precipitating phases in the remaining conditions were found to form with a wavy, interconnected morphology that resulted in a film-like covering across the grain boundary. With the exception of conditions G and H, the re-precipitation of γ′ was also observed around the grain boundaries in conditions D, E, F, and I, resulting in localised distributions of tertiary γ′. Analysis of the XRD data indicated that the precipitating phases in samples D-I were M_6C and $M_{23}C_6$.

The XRD data collected at room temperature from each sample were analyzed using the Pawley method [14] in TOPAS-academic, which also allowed the lattice parameters of the γ and γ′ phases from each condition to be obtained. In all cases, the γ lattice parameter was found to be 3.59Å, whereas the lattice parameter of the γ′ phase was 3.60Å, resulting in a lattice misfit of ~0.28% for all conditions.

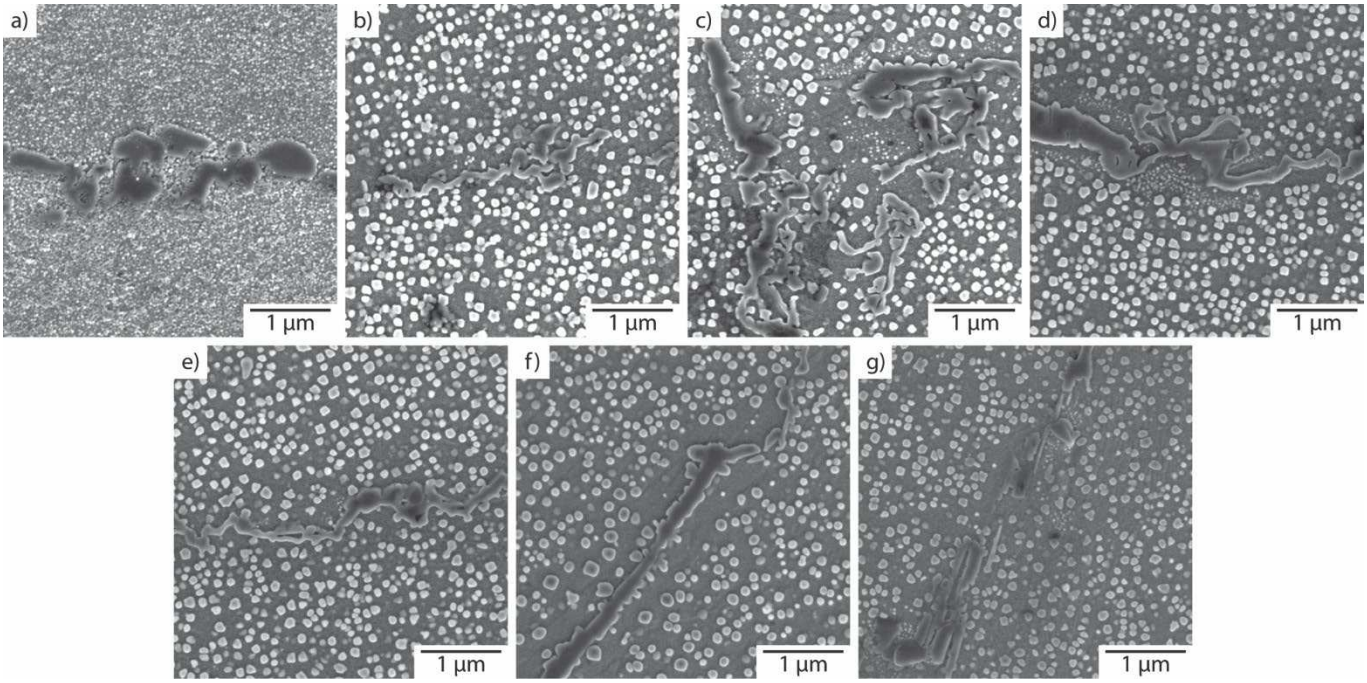

Figure 3: Secondary electron micrographs of grain boundary precipitation, a-g) correspond to material subjected to C-I respectively.

ETMT Testing

The results obtained from ETMT tensile testing are shown in Figure 4. Marked differences were seen in the mechanical performance of samples subjected to the different heat-treatments. Condition C was found to result in the highest yield strength. Conditions D, E & F, which did not involve an intermediate ageing treatment, showed lower yield strength compared to the conditions that involved a two-step ageing treatment (G & H). Table 4 provides a summary of the tensile properties for each condition as compared to the data provided by Haynes for cast and cold rolled material in a standard sheet form tested at 927˚C (i.e. heat-treated at 1150˚C for 1 hour, followed by 1010˚C for 2 hours and 788˚C for 8 hours) [6]. It is noted that the comparison with data collected from bulk material is not ideal as miniature samples are more sensitive to localised effects, which produce larger statistical scatter in measured properties. Furthermore, ETMT data, in particular elongation data, is unreliable following the onset of necking (yield), and hence the reader is advised to exercise caution when comparing these data. Nevertheless, the comparison with rolled material was deemed the most appropriate as the standard test pieces used for the qualification of the mechanical properties of sheet material are of a reduced volume compared to other forms, such as forged billets. This makes these data more comparable to the LPBF material which has been produced in similar section thicknesses.

Following ETMT testing, the fracture surfaces of the samples were analysed using both optical and scanning electron microscopy. Cracking and cavitation were found to occur along the grain boundaries of all samples tested. However, no significant differences between the cracking density were observed. In addition, the carbide/boride network and the γ′ distributions were not found to differ significantly in the vicinity of the tensile fracture surfaces.

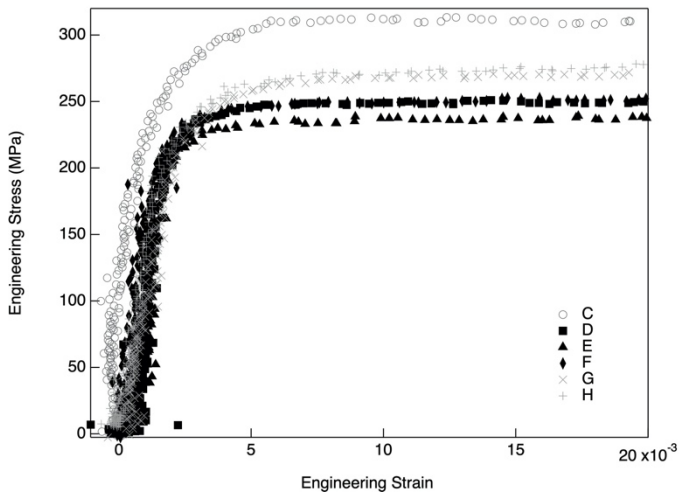

Figure 4: Engineering stress-strain curves obtained from ETMT tensile testing

*Table 4: Tensile properties from ETMT tensile testing. *From the Haynes 282 data sheet for 927 ˚C [6].*

Condition	Yield Strength (MPa)	UTS (MPa)	Elongation (%)
C	300	330	23
D	230	250	22
E	220	240	26
F	230	250	34
G	260	270	34
H	260	280	30
H282 sheet*	303	346	37

Accelerated creep testing was also performed at ~900 ˚C, under a load of 120 MPa to enable comparison with existing published data [6]. Note that the load chosen is not representative of service conditions. The collective set of results are shown in Figure 5a. Samples subjected to heat treatments E and G displayed very short creep lives of ~30 hours. Conditions C, D and H exhibited lives between 70 to 130 hours. The tests for condition F (not shown in Figure 5a) cannot be compared to the other conditions as one of the tests was performed at a load of 100 MPa, and the second test, although performed at 120 MPa, showed an unusual current profile suggesting that the temperature was significantly lower than 900˚C.

Figure 5b shows a magnified region of the creep curves, in particular with respect to the secondary creep rates of the samples. Secondary creep rates are considered to be a more reliable metric of comparison as the overall creep life in such miniature tests is often affected by defects within the microstructure such as nanoporosity. These data confirm that conditions E and G displayed the lowest secondary creep rates, whereas the remaining conditions, with the exception of one of the repeats for condition H, showed a similar slope, and hence secondary creep rate. It is noted that the two repeat tests for condition D, displayed near-identical secondary creep rates.

The microcracking behaviour near the creep fracture surfaces was also examined using optical microscopy and SEM. No significant differences between the cracking density could be observed. As with the tensile specimens, cavitation and cracking were found to occur along the grain boundaries. SEM was used to obtain higher resolution images of the interaction of cracking with the grain boundary structure, and representative images from condition H are shown in Figure 6. The γ′ structure was found to exhibit the characteristic alignment that is typically observed in crept specimens. Furthermore, cracking and cavitation were found along the grain boundary phases, and in particular at the interfaces between the matrix and the carbides/borides. Importantly, the post-mortem analysis did not reveal significant intragranular oxidation that would compromise the creep performance. However, additional high-resolution microscopy is required to characterise the effect of elemental oxygen or the formation of nanoscale oxides along the grain boundaries and their subsequent effects on the creep properties.

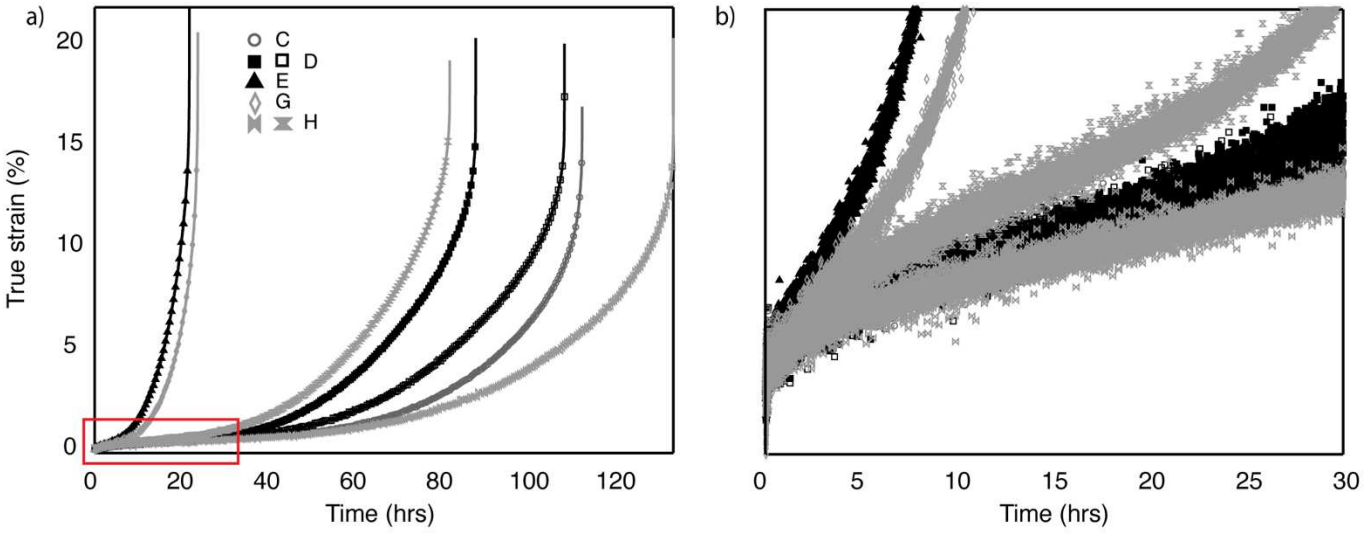

Figure 5: Creep curves to failure (left) and expanded detail of the outlined area providing a detailed view of secondary creep (right)

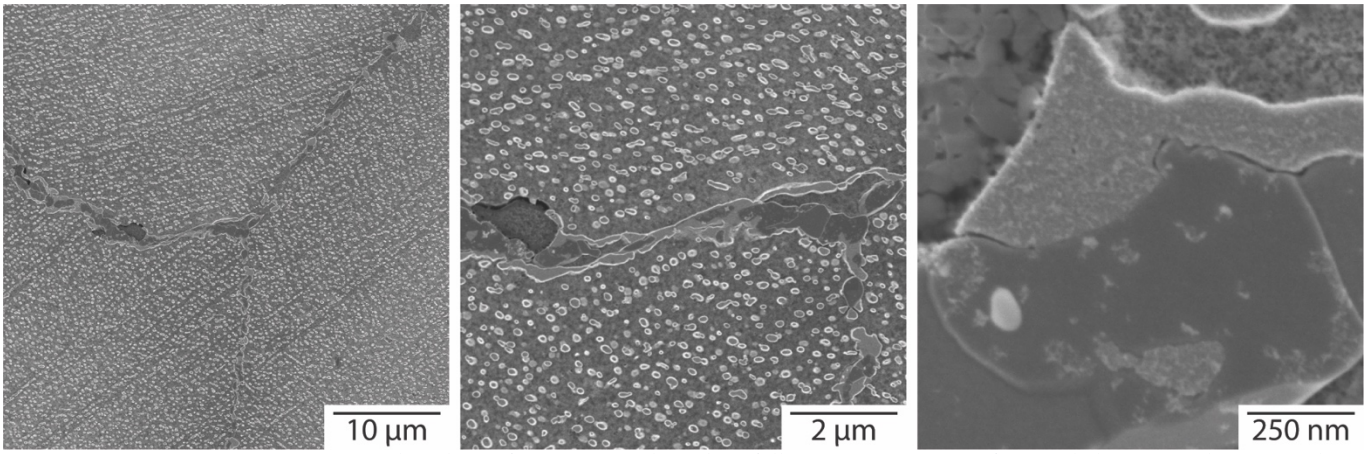

Figure 6: Representative microstructural analysis of cavitation and cracking following creep testing of a sample heat-treated using condition H

Long Duration Stability

In order to understand the evolution of the microstructure following long exposures at the operating temperature, samples of the as-deposited material as well as samples heat-treated using conditions B, D and H were encapsulated in Ar-backfilled quartz ampoules and subjected to 1000 hours at 850˚C.

The microstructures of the samples after the long duration exposure were found to be similar, consisting of three grain boundary phases and a coarsened monomodal γ′ distribution. The microstructures only differed in the carbide morphologies, as discrete carbides were found in the as-deposited sample and the sample heat-treated using condition B, whereas a more continuous carbide morphology, consistent with those shown in Figure 3, was observed in samples heat-treated using condition D and H. Figure 7 shows a representative set of EDX results obtained from the samples heat-treated following condition B. The grain boundary phases consisted primarily of a bright, blocky phase and a light grey phase. In addition, a dark lenticular phase was also found to form at the interfaces with the bright contrast phase, however, this phase was only observed in small volume fractions. The EDX maps shown in Figure 7 indicated that the bright phase was enriched in Mo and depleted in Cr compared to the surrounding matrix, whereas the light grey phase was enriched in Cr. Further analysis of the phases provided an approximate composition for the bright phase of ~40Ni-20Mo-20Cr-10Co (at.%) with trace contents of Al, Ti and Si, consistent with the M_6C phase. In contrast, the dull grey phase was found to have a composition of ~50 Cr-30Ni-10Mo (at.%) and small concentrations of Co, Al, Ti and Si, consistent with the $M_{23}C_6$ phase. The γ′ distributions were also analyzed using the log normal method [CITE] and the mean γ′ size was found to be ~150-200 nm.

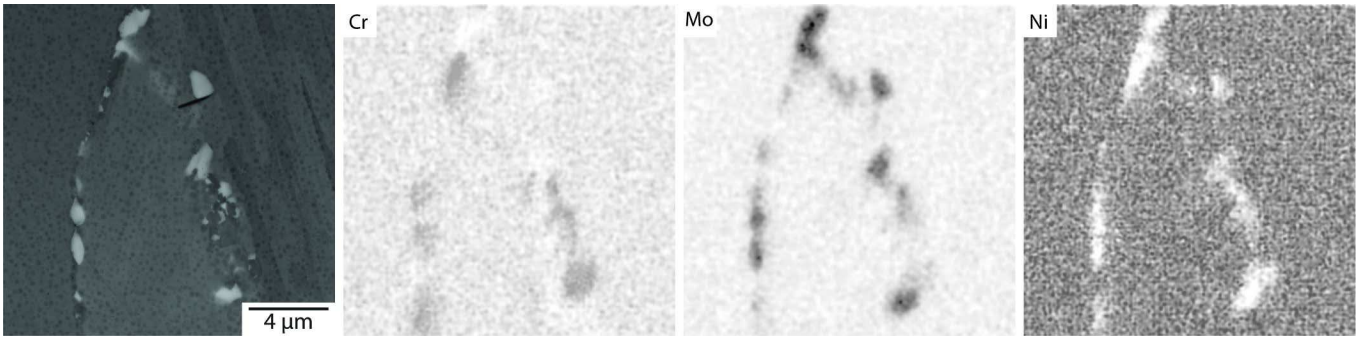

Figure 7: EDX maps of Cr, Mo and Ni obtained from the sample heat-treated using condition B and exposed at 850 ˚C for 1000 hours. Note that the colouring in the image is inverted and hence black regions indicate elemental enrichment, whereas white areas signify elemental depletion.

Discussion

The key aim of this study was to determine an ageing procedure for H282 manufactured through LPBF that provided a good compromise between the material properties and the cost/duration of the heat-treatment. However, before the ageing heat-treatment for the material could be determined, it was vital that a recrystallization temperature was defined. A recrystallized grain structure is desirable as it provides an isotropic state that facilitates lifing operations.

The recommended heat-treatment for cast material to both recrystallize the grain structure and optimize the carbide distributions, is a solutioning step at 1150˚C for 1 hour, followed by a two-step ageing heat-treatment at 1010˚C for 2 hours and 788˚C for 8 hours [6]. This standard heat treatment results in microstructures that comprise large Ti-rich MC/MN particles, $M_{23}C_6$ and/or M_6C carbides along the grain boundaries and a monomodal γ′ distribution [7, 9]. A similar heat-treatment was performed on a sample of as-

deposited LPBF-H282, Figure 1. However, it was clear from the results presented in Figure 2, that the solution temperature of 1150˚C was insufficient to induce recrystallization. Several solution heat-treatments were explored, and the lowest temperature at which recrystallization proceeded to completion was 1240˚C but required a 2-hour exposure. Thus, in the interest of minimizing process time, a 1-hour exposure at 1250˚C was selected as the preferred recrystallization heat-treatment.

In several AM superalloys, recrystallization has been found to be closely linked to the γ′ behavior, with fully recrystallized microstructures achieved at temperatures very near the γ′ solvus temperature [3, 18]. However, this behavior was not observed in H282, as the γ′ solvus temperature was found to be ~ 1000˚C, and hence, well under the recrystallization temperatures of 1240-1250˚C. It might, therefore, be reasonable to assume that the behavior is governed by the carbide/boride distributions at the cellular colonies. These carbides are believed to exert a drag pressure on the boundaries, increasing the activation energy required for recrystallization.

One strategy that has successfully reduced the recrystallization temperature in alloy IN738LC, is the use of a lower temperature, stress relieving step prior to the high temperature step [19]. Messé *et al.* [19] attributed the reduction in the recrystallization temperature to the metastability of the carbides, and the transformation occurring during the stress relieving step that results in $M_{23}C_6$ carbides being dissolved during the high temperature heat-treatment. A similar strategy was also explored for H282, although the results are not presented herein. Two stress relieving temperatures were trialled, 900˚C and 1010˚C for 12 hours each, followed by a high temperature exposure at 1190˚C for 1 hour. In both cases the fraction of recrystallized material did not increase compared to the exposure at 1190˚C.

Following the determination of a recrystallisation temperature, a range of heat-treatments (Table 2) with defined cooling rates were investigated to explore to what extent the γ′ distribution and carbides could be manipulated. Condition C utilized gas fan quenching between each ageing step to obtain a fine γ′ distribution. In conditions D-F, the intermediate ageing step at 1010˚C was eliminated, and the effect of the solution heat-treatment was evaluated on the material properties, and in particular for condition E this was designed to include a small fraction of un-recrystallized grains. However, all samples heat-treated using condition E were found to exhibit fully recrystallized microstructures. In conditions G-I, the temperature of the intermediate ageing step was varied to elucidate the stability and crystallography of the resulting carbides.

Typical microstructures from each heat-treatment are shown in Figure 3. As anticipated, the microstructure in the sample heat-treated using condition C consisted of a finer γ′ distribution compared to all other conditions, which were found to have largely equivalent γ′ distributions, Table 3. Furthermore, all samples showed extensive carbide precipitation along the grain boundaries. The carbide species were identified using XRD to be the M_6C and $M_{23}C_6$ in conditions D-I. M_6C carbides and M_3B_2 borides were identified in condition C. However, it was the tertiary γ′ behavior around the carbides that was found to differ between samples. Notably, whilst most conditions showed fine, tertiary γ′ around carbides, no such precipitation was observed in conditions G and H, for which the intermediate ageing temperature was altered to be 900 and 990˚C respectively. For conditions D-F, no intermediate ageing step was used, thereby allowing the nucleation of γ′ on cooling to the 788˚C ageing temperature. This led to a near-bimodal γ′ distribution being observed with the tertiary γ′ forming around the carbides. This behavior was also believed to occur in condition I as the intermediate ageing step at 1010˚C is above the γ′ dissolution determined by DSC. In contrast, for conditions G and H, the intermediate ageing step was carried out at a temperature at which the γ′ is already present, hence, growth occurred at these intermediate temperatures resulting in a monomodal γ′ distribution of ~100 nm in size upon further exposure at 788˚C. This result was found to be significantly different to the EBM results reported by Unocic *et al.* [11], in which the γ′ distribution in heat-treated samples reprecipitated following the 788˚C exposure with a mean size of ~20-30 nm. Further work is therefore required to understand the origins of the increased γ′ coarsening kinetics in LPBF material.

In order to extract further insights into the behavior of the material with respect to the different heat-treatments outlined in Table 2, a series of mechanical tests were performed using ETMT at ~900˚C and a strain rate of $1x10^{-5}$ s^{-1}. The tensile properties obtained from the material heat-treated following condition C were found to be superior to the remaining conditions due to the fine γ′ distribution observed in this sample. The data acquired from this condition were found to be in good agreement with the data provided by Haynes for sheet material [6], as shown in Table 4. The tensile properties of the remaining conditions were found to be largely equivalent, but inferior to condition C, reflecting the similarities observed in the microstructures of these samples.

In addition to tensile testing, creep testing at ~900˚C and ~120MPa was also performed on the ETMT and the results are summarized in Figure 5. Conditions E and G exhibited the shortest creep lives of ~30 hours, whereas the remaining conditions (C, D and H), displayed lives in the range of 70-120 hours. As a result of the choice of parameters for creep testing to be completed within 100 hours, the likely creep mechanisms in operation in these tests will by dominated by the grain boundary characteristics rather than the intragranular microstructure. Due to the size of the samples relative to the grain structure of the material, a variation in the creep lives obtained through ETMT of up to ~30 % can be expected, and hence, the results obtained for conditions C, D and H were found to be within error of the ~100 hour creep rupture life expected. However, post-mortem examination of conditions E and G did not reveal any areas to warrant the tests invalid and hence the low creep lives obtained in these samples are believed to be related to the matrix and grain boundary character. Nevertheless, the results were difficult to interpret as little correlation with the microstructures shown in Figure 3 was observed. Due to the small sample sizes used in the ETMT, the effect of oxidation along the grain boundaries is often a concern and could obscure the bulk material behavior. However, the post-mortem analysis did not reveal any significant oxidation effects along the grain boundaries. Therefore, in order to elucidate the creep behavior of the samples, additional high-resolution microscopy and characterization of the grain boundaries is required as some weak evidence shows a slight dependence on the final cooling rate employed following heat-treatment. Evidence from wrought H282 suggests that the creep rupture strength of the alloy is critically dependent on the Mo content [7], with significant decline in the creep life when the Mo content varies by ±

1 wt.% from the optimum 8.5 wt.%. It is possible that given the stability of the M_6C carbides found in LPBF H282, the Mo concentration within the matrix is lower than the optimum level, and hence further studies are required to study this effect in greater detail. Although the ETMT data provides a useful self-consistent ranking tool of the different heat-treatment conditions, full scale creep testing as well as additional creep conditions would also be beneficial in order to understand the creep behavior of the material in detail. Lastly, whilst the data demonstrates the variability that may be obtained in the creep performance of the alloy as a function of the heat-treatment and cooling rate, it also reassuringly shows that properties which are equivalent to the conventionally produced alloy are readily achievable.

Ultimately, the behavior of the material will be governed by the resulting microstructure following prolonged exposure at the service temperature. To this end, the long duration microstructural stability of the material at 850˚C was examined and it was found that regardless of the starting condition the resulting microstructures consisted of a monomodal γ′ distribution with sizes of ~150-200 nm and the M_6C and $M_{23}C_6$ carbides, although the starting condition determined the morphology of the carbides. This behavior demonstrates the propensity of the material to achieve thermodynamic equilibrium. Additional microstructural analysis at different time intervals would be useful in order to determine the minimum time at temperature that the material requires to reach equilibrium. In addition, full-scale mechanical tests of samples in this state would be invaluable in determining the useful life of the component.

Conclusions

The microstructure and properties of alloy H282 produced through LPBF were investigated as a function of the post-deposition heat-treatment and compared to those of conventionally produced material. The initial microstructures of the alloy in the as-deposited state as well as following a heat-treatment of 1150˚C/1 hour + 1010˚C/4 hours + 788˚C/8 hours, were investigated and the formation of the M_6C and $M_{23}C_6$ carbides were identified, instead of the more widely reported MC/MN particles in cast material. The presence of these carbides in the as-deposited state was found to be critical to the recrystallisation of the alloy. A minimum temperature of 1240˚C (for 2 hours) was required to fully recrystallize the alloy due to the additional energy barrier for the redistribution of the carbides. The microstructures were also investigated following a series of heat-treatments in order to explore the extent to which the γ′ distribution and carbide formation could be manipulated. The resulting microstructures were found to be equivalent, producing coarsened grain boundary M_6C and $M_{23}C_6$ carbides and an intragranular monomodal γ′ distribution of ~100 nm, with the exception of the material for which fast cooling was used, which resulted in a much finer γ′ distribution. Tertiary γ′ was found to precipitate in the vicinity of the carbides along the grain boundaries in all conditions for which a γ′ super-solvus step preceded the ageing step at 788˚C. Tensile and creep properties were evaluated using ETMT testing at ~900˚C. The tensile properties of the material following each heat-treatment were found to be analogous and in agreement with the minimal differences observed in the microstructures. In contrast, significant differences were observed in the creep behavior following the different heat-treatments, although no correlation with the microstructures could be found, indicating that additional high-resolution characterization of the grain boundary character and composition is required. However, the data showed that properties equivalent to conventionally produced H282 may be obtained in LPBF produced material provided a suitable heat-treatment is chosen. Lastly, the microstructures of the material following long duration exposures at 850˚C exhibited a monomodal γ′ distribution with a mean size of ~150-200 nm and M_6C and $M_{23}C_6$, the morphology of which was dependent on the starting condition.

Acknowledgements

This work was financially and in-kind supported by Rolls-Royce plc and was conducted in its entirety at the University of Cambridge and at Rolls-Royce plc. Mrs Sue Rhodes is gratefully acknowledged for laboratory assistance.

Bibliography

[1] L.E. Murr, Frontiers of 3D Printing/Additive Manufacturing: from Human Organs to Aircraft Fabrication†, Journal of Materials Science & Technology 32(10) (2016) 987-995.
[2] P. Han, Additive Design and Manufacturing of Jet Engine Parts, Engineering 3(5) (2017) 648-652.
[3] V.D. Divya, R. Muñoz-Moreno, O.M.D.M. Messé, J.S. Barnard, S. Baker, T. Illston, H.J. Stone, Microstructure of selective laser melted CM247LC nickel-based superalloy and its evolution through heat-treatment, Materials Characterization 114 (2016) 62-74.
[4] X. Wang, L.N. Carter, B. Pang, M.M. Attallah, M.H. Loretto, Microstructure and yield strength of SLM-fabricated CM247LC Ni-Superalloy, Acta Materialia 128 (2017) 87-95.
[5] C. Körner, Additive manufacturing of metallic components by selective electron beam melting — a review, International Materials Reviews 61(5) (2016) 361-377.
[6] Haynes International, HAYNES 282 Alloy Data Sheet, access via: http://haynesintl.com/docs/default-source/pdfs/new-alloy-brochures/high-temperature-alloys/brochures/282-brochure.pdf?sfvrsn=20
[7] L.M. Pike, Development of a fabricable gamma-prime (γ′) strengthened superalloy, in: R.C. Reed, K.A. Green, P. Caron, T.P. Gabb, M.G. Fahrmann, E.S. Huron, S.A. Woodard (Eds.) Superalloys 2008, TMS, Seven Springs, PA, USA, 2008.
[8] L.M. Pike, 100+ years of wrought alloy development at Haynes International, in: E. Ott, A. Banik, X. Liu, I. Dempster, K. Heck, J. Andersson, J. Groh, T. Gabb, R. Helmink, A. Wusatowska-Sarnek (Eds.) 8th International Symposium on Superalloy 718 and Derivatives, TMS, 2014, pp. 15-30.
[9] K.A. Unocic, D. Shin, X. Sang, E. Cakmak, P.F. Tortorelli, Single-step aging treatment for a precipitation-strengthened Ni-based alloy and its influence on high-temperature mechanical behavior, Scripta Materialia 162 (2019) 416-420.

[10] L.M. Pike, Long term thermal exposure of Haynes 282 alloy, in: E.A. Ott, G.J. R., I. Dempster, T.P. Gabb, R. Helmink, X. Liu, A. Mitchell, G.P. Sjöberg, A. Wusatowska-Sarnek (Eds.) 7th International Symposium on Superalloy 718 and Derivatives, TMS, 2010.
[11] K.A. Unocic, M.M. Kirka, E. Cakmak, D. Greeley, A.O. Okello, S. Dryepondt, Evaluation of additive electron beam melting of haynes 282 alloy, Materials Science and Engineering: A (2019).
[12] W.J. Boettinger, U.R. Kattner, K.W. Moon, J.H. Perepezko, DTA and Heat-flux DSC measurements of alloy melting and freezing, NIST Recommended Practice Guides, National Institute of Standards and Technology, 2006.
[13] G.F. Vander Voort, G.M. Lucas, E.P. Manilova, Metallography and microstructures of heat-resistance alloys, ASM Handbook, Volume 9: Metallography and Microstuctures, 2004, pp. 820-859.
[14] G.S. Pawley, Uni-cell refinement from powder diffraction scans, J. Appl. Cryst. 14 (1981) 357-361.
[15] B. Roebuck, D.C. Cox, R.C. Reed, An innovative device for the mechanical testing of miniature specimens of superalloys, in: K.A. Green, T.M. Pollock, H. Harada, T.E. Howson, R.C. Reed, J.J. Schirra, S. Walston (Eds.) Superalloys 2004, TMS, Seven Springs, PA, USA, 2004.
[16] H. Matysiak, M. Zagorska, J. Andersson, A. Balkowiec, R. Cygan, M. Rasinski, M. Pisarek, M. Andrzejczuk, K. Kubiak, K.J. Kurzydlowski, Microstructure of Haynes((R)) 282((R)) Superalloy after Vacuum Induction Melting and Investment Casting of Thin-Walled Components, Materials (Basel) 6(11) (2013) 5016-5037.
[17] A.J. Goodfellow, E.I. Galindo-Nava, K.A. Christofidou, N.G. Jones, T. Martin, P.A.J. Bagot, C.D. Boyer, M.C. Hardy, H.J. Stone, Gamma Prime Precipitate Evolution During Aging of a Model Nickel-Based Superalloy, Metallurgical and Materials Transactions A 49(3) (2017) 718-728.
[18] R. Muñoz-Moreno, V.D. Divya, S.L. Driver, O.M.D.M. Messé, T. Illston, S. Baker, M.A. Carpenter, H.J. Stone, Effect of heat-treatment on the microstructure, texture and elastic anisotropy of the nickel-based superalloy CM247LC processed by selective laser melting, Materials Science and Engineering: A 674 (2016) 529-539.
[19] O.M.D.M. Messé, R. Muñoz-Moreno, T. Illston, S. Baker, H.J. Stone, Metastable carbides and their impact on recrystallisation in IN738LC processed by selective laser melting, Additive Manufacturing 22 (2018) 394-404.